Geophysical Research Letters

MMS Measurements of the Vlasov Equation: Probing the Electron Pressure Divergence Within Thin Current Sheets

J. R. Shuster[1,2] [ID]**, D. J. Gershman[2]** [ID]**, L.-J. Chen[2]** [ID]**, S. Wang[1,2]** [ID]**, N. Bessho[1,2]** [ID]**, J. C. Dorelli[2],**
D. E. da Silva[2,3,4] [ID]**, B. L. Giles[2]** [ID]**, W. R. Paterson[2]** [ID]**, R. E. Denton[5]** [ID]**, S. J. Schwartz[6]** [ID]**,**
C. Norgren[7] [ID]**, F. D. Wilder[6]** [ID]**, P. A. Cassak[8]** [ID]**, M. Swisdak[9]** [ID]**, V. Uritsky[2,10]** [ID]**, C. Schiff[2],**
A. C. Rager[2,10] [ID]**, S. Smith[2,10]** [ID]**, L. A. Avanov[1,2]** [ID]**, and A. F. Viñas[2]**

[1]Department of Astronomy, University of Maryland, College Park, MD, USA, [2]NASA Goddard Space Flight Center, Greenbelt, MD, USA, [3]Trident Vantage Systems, Greenbelt, MD, USA, [4]Whiting School of Engineering, Johns Hopkins University, Baltimore, MD, USA, [5]Department of Physics and Astronomy, Dartmouth College, Hanover, NH, USA, [6]Laboratory for Atmospheric and Space Physics, University of Colorado Boulder, Boulder, CO, USA, [7]Birkeland Centre for Space Science, Department of Physics and Technology, University of Bergen, Bergen, Norway, [8]Department of Physics and Astronomy, West Virginia University, Morgantown, WV, USA, [9]Institute for Research in Electronics and Applied Physics, University of Maryland, College Park, MD, USA, [10]Department of Physics, Catholic University of America, Washington, DC, USA

Abstract We investigate the kinetic structure of electron-scale current sheets found in the vicinity of the magnetopause and embedded in the magnetosheath within the reconnection exhaust. A new technique for computing terms of the Vlasov equation using Magnetospheric Multiscale (MMS) measurements is presented and applied to study phase space density gradients and the kinetic origins of the electron pressure divergence found within these current sheets. Crescent-shaped structures in $\nabla_{\perp 2} f_e$ give rise to bipolar and quadrupolar signatures in $\mathbf{v} \cdot \nabla f_e$ measured near the maximum $\nabla \cdot \mathbf{P}_e$ inside the current layers. The current density perpendicular to the magnetic field is strong ($J_\perp \sim 2$ μA/m^2), and the thickness of the current layers ranges from 3 to 5 electron inertial lengths. The electron flows supporting the current layers mainly result from the combination of $\mathbf{E} \times \mathbf{B}$ and diamagnetic drifts. We find nonzero $\mathbf{J} \cdot \mathbf{E}'$ within the current sheets even though they are observed apart from typical diffusion region signatures.

Plain Language Summary We discovered how to use data from outer space to measure what is known as the Vlasov equation, held by many to be the most important equation in plasma physics. Beginning with Ludwig Boltzmann's insights from the late 1800s regarding microscopic motions of ordinary gases, Anatoly Vlasov in 1945 applied Boltzmann's ideas to understand the nature of electrified gases called plasmas. What has prevented researchers from measuring the Vlasov equation for over 100 years since Boltzmann? The difficulty is that Vlasov's equation lives in phase space, which enlists no less than seven dimensions — three for position (x, y, z), three for velocity (v_x, v_y, v_z), and one for time (t) — thus, for over a century, no experiment has been designed to sufficiently and accurately resolve each of these dimensions. Today, instruments comprising the revolutionary Fast Plasma Investigation onboard NASA's four spacecraft Magnetospheric Multiscale mission, flying over 40,000 miles away from Earth through regions where the magnetic fields of the Earth and Sun collide, equip space scientists with data collected at higher resolution than ever before achieved — high enough to at last resolve terms in the Vlasov equation for the first time in history, which we demonstrate here.

1. Introduction

Elucidating the kinetic dynamics of thin current sheet equilibria is essential for understanding many fundamental plasma energization phenomena, such as the onset of magnetic reconnection, plasma turbulence, and wave instabilities (Harris, 1962; Priest, 1976; Daughton, 2002; Sundkvist et al., 2007). Detection of electron-scale current sheets in Earth's magnetic environment has become possible with the high-resolution instrumentation onboard the Magnetospheric Multiscale (MMS) spacecraft, which can resolve electron skin depth (d_e) scale, filamentary currents narrower than the spacecraft separation (Phan et al., 2016; Phan et al.,

2018; Yordanova et al., 2016; Wilder et al., 2017). Current sheets with thicknesses on the order of a few d_e are often observed in association with the electron diffusion region (EDR) and separatrix regions of magnetic reconnection (Burch et al., 2016; Chen et al., 2016; Chen et al., 2017; Genestreti et al., 2018; Norgren et al., 2016; Torbert et al., 2016; Torbert et al., 2018; Wang et al., 2018; Webster et al., 2018). Recent studies have shown that thin current sheets and their associated electron crescent distributions can result purely as a manifestation of diamagnetic effects (Egedal et al., 2016; Rager et al., 2018), though these are typically found in regions where there is significant dissipation (Eriksson et al., 2016; Torbert et al., 2017; Genestreti et al., 2017; Wilder et al., 2018). We present three examples of thin current sheets that do not exhibit clear evidence of local reconnection, since they occur within the exhaust downstream of the magnetopause X-line without typical EDR signatures.

To investigate the kinetic structure of the current sheets, we develop a technique to visualize the spatial gradient term in the Vlasov equation for the first time using MMS data. One of the most important equations in plasma physics, the Vlasov equation self-consistently relates the plasma phase space density to the electric and magnetic forces present in the system, and it is widely employed to describe the kinetic evolution of collisionless plasmas, such as those occurring naturally in Earth's magnetic environment, near the Sun, and throughout the solar system. Though often used effectively in theoretical contexts, terms of the Vlasov equation are difficult to measure directly. MMS's Fast Plasma Investigation (FPI) captures three-dimensional electron distributions every 30 ms and ion distributions every 150 ms at each of the four spacecraft (Pollock et al., 2016), offering unprecedented spatiotemporal and velocity space resolution that permits computation of terms in the Vlasov equation for electrons. We apply this novel methodology to determine the regions of electron velocity space that drive variations in the divergence of the electron pressure tensor.

2. Methods

2.1. Event Search Criteria and Current Sheet Thickness Determination

In search of strong current layers capable of supporting electron crescent distributions, such as those recently observed and modeled in association with the EDR of magnetic reconnection (e.g., Burch et al., 2016; Bessho et al., 2016), we searched 2 years of Phase 1 (dayside) MMS data for strong perpendicular current density $J_\perp$ measurements. To ensure that the FPI moments were computed with sufficient accuracy, we set lower and upper limits on the electron number density n_e to minimize undercounting and saturation. With these two criteria: $J_\perp > 1\mu A/m^2$ and $2\ cm^{-3} < n_e < 50\ cm^{-3}$, our search yielded nearly 2,000 candidate events. We next filtered these events based on visual inspection of the kinetic electron distribution function structures associated with each current layer. In this work, we focus on three of these events where the strong current feature is thin (on the order of a few d_e) and found isolated in the magnetosheath (MSH) reconnection exhaust far downstream from the diffusion region. Events 1, 2, and 3 refer to these three events which occurred in 2016 on November 28, December 23, and December 27, respectively.

Four-spacecraft timing analysis is used to estimate the current sheet speed and thickness. Assuming the structure moves at speed V along the normal direction $\mathbf{n}$, we solve for V and $\mathbf{n}$ by inverting the linear system: $(\mathbf{r}_i - \mathbf{r}_1) \cdot \mathbf{n} = V(t_i - t_1)$ and $|\mathbf{n}| = 1$, where we let $i = \{2, 3, 4\}$ for MMS 2, 3, and 4, respectively, $\mathbf{r}_i$ denotes the position of the ith spacecraft, t_i specifies the time of maximum $J_\perp$ observed by the ith spacecraft, and MMS 1 is arbitrarily taken as the reference spacecraft (e.g., Harvey, 1998). For each event, the FWHM time duration of the current structure is on the order of 0.1 s, the local d_e is about 1.5 km, and the current sheet thickness is estimated to be about 3 to 5 d_e. These thicknesses are on the order of the thermal electron gyroradii, which are 1.5, 1.3, and 1.2 km for Events 1, 2, and 3, respectively.

2.2. Method for Estimating Terms in the Vlasov Equation With FPI

Modern studies and applications of collisionless plasma phenomena require the kinetic description provided by the Vlasov equation (e.g., Nicholson, 1983; Califano et al., 2016; Gershman et al., 2017). We utilize the Vlasov equation describing the evolution of the electron distribution function f_e in phase space

$$\frac{df_e}{dt} = \frac{\partial f_e}{\partial t} + \mathbf{v} \cdot \nabla f_e + \frac{\mathbf{F}}{m} \cdot \nabla_\mathbf{v} f_e = 0, \tag{1}$$

where $\mathbf{F} = -e(\mathbf{E} + \mathbf{v} \times \mathbf{B})$ is the Lorentz force (e.g., Gurnett & Bhattacharjee, 2005). The spatial gradient term ∇f_e represents the kinetic origin of the electron pressure divergence via the following integral relationship:

$$m_e \int \mathbf{v}(\mathbf{v} \cdot \nabla f_e) d^3v = \nabla \cdot \mathbf{P}_e + \nabla \cdot (m_e n_e \mathbf{U}_e \mathbf{U}_e). \tag{2}$$

For the events in this study, the inertial term $\nabla \cdot (m_e n_e \mathbf{U}_e \mathbf{U}_e)$ in equation (2) is an order of magnitude smaller than $\nabla \cdot \mathbf{P}_e$. Thus, determination of the spatial gradient ∇f_e as a function of $\mathbf{v}$ provides a direct measure of how structures in the electron velocity distribution relate to changes in the divergence of the electron pressure tensor. The temporal and velocity space gradient terms in equation (1) are not considered in this study since they do not contribute to $\nabla \cdot \mathbf{P}_e$. Computing ∇f_e from the four spacecraft skymaps is most straightforward in Cartesian coordinates. For a given quantity Q_1 measured by MMS 1 at position $\mathbf{x}_1$ in Geocentric Solar Ecliptic (GSE) coordinates, we use the known separations between MMS 1 and the nth spacecraft ($\Delta \mathbf{x}_n = \mathbf{x}_n - \mathbf{x}_1$) to Taylor expand about MMS 1 to first order

$$Q_n \approx Q_1 + \frac{\partial Q}{\partial x} \Delta x_n + \frac{\partial Q}{\partial y} \Delta y_n + \frac{\partial Q}{\partial z} \Delta z_n, \tag{3}$$

where $n = \{2, 3, 4\}$. Equation (3) treats $\partial Q/\partial x$, $\partial Q/\partial y$, and $\partial Q/\partial z$ as constants which can be readily obtained by solving the system

$$\begin{bmatrix} (x_2 - x_1) & (y_2 - y_1) & (z_2 - z_1) \\ (x_3 - x_1) & (y_3 - y_1) & (z_3 - z_1) \\ (x_4 - x_1) & (y_4 - y_1) & (z_4 - z_1) \end{bmatrix} \cdot \begin{bmatrix} \frac{\partial Q}{\partial x} \\ \frac{\partial Q}{\partial y} \\ \frac{\partial Q}{\partial z} \end{bmatrix} = \begin{bmatrix} Q_2 - Q_1 \\ Q_3 - Q_1 \\ Q_4 - Q_1 \end{bmatrix}. \tag{4}$$

This procedure is the same used to calculate spatial derivatives needed for various multispacecraft analysis techniques, such as the curlometer estimation of the current density from four-spacecraft magnetic field measurements, timing analysis, and the divergence of the pressure tensor (e.g., Harvey, 1998). To obtain gradients of electron phase space density, we let $Q = f_e$ in equation (4). At time t, we apply the same procedure to *each* of the FPI skymap bins, that is, we let $Q = f_e^{i,j,k} = f_e(E_i, \theta_j, \phi_k, t)$ for bin (i, j, k), and we then solve for $(\partial f_e^{i,j,k}/\partial x)$, $(\partial f_e^{i,j,k}/\partial y)$, and $(\partial f_e^{i,j,k}/\partial z)$, where E_i, θ_j, and ϕ_k are the energy, polar angle, and azimuthal angle corresponding to bin (i, j, k), respectively (Shuster et al., 2019).

MMS distribution functions are commonly visualized as slices of the full distribution (i.e., only a planar subset of the available velocity space bins is plotted) projected onto field-aligned coordinates. In order to ensure $f_{i,j,k}$ for each spacecraft corresponds to the same portion of velocity space, we first compute the gradient of the phase space densities in their original GSE frame *before* rotating to field-aligned coordinates, since the field-aligned coordinate system will in general differ between spacecraft. Additionally, since f_e is sampled by the four spacecraft at different times and at different ϕ locations, we linearly interpolate the skymaps in both time and azimuth. Since the potential difference between spacecraft is at most about 1 V for these events, interpolation in energy is unnecessary. In principle, since FPI has 32 energy bins, 16 polar angle bins, and 32 azimuthal bins, this procedure yields a three-component vector derivative for each of the $32 \times 16 \times 32 = 16,384$ velocity space sectors sampled by FPI, though in practice many of these bins measure 0 counts and can be neglected. Once ∇f_e is estimated, we evaluate the spatial gradient term appearing in the Vlasov equation $\mathbf{v} \cdot \nabla f_e$ for the $(i, j, k)^{\text{th}}$ bin as follows:

$$(\mathbf{v} \cdot \nabla f_e)^{i,j,k} = v_x^{i,j,k} \cdot \frac{\partial f_e(E_i, \theta_j, \phi_k)}{\partial x} + v_y^{i,j,k} \cdot \frac{\partial f_e(E_i, \theta_j, \phi_k)}{\partial y} + v_z^{i,j,k} \frac{\partial f_e(E_i, \theta_j, \phi_k)}{\partial z}, \tag{5}$$

where the Cartesian velocity space coordinates of the (i, j, k)th bin in the nonrelativistic limit are as follows:

$$v_x^{i,j,k} = -\sqrt{2E_i/m_e} \sin(\theta_j) \cos(\phi_k), \tag{6}$$

$$v_y^{i,j,k} = -\sqrt{2E_i/m_e} \sin(\theta_j) \sin(\phi_k), \tag{7}$$

$$v_z^{i,j,k} = -\sqrt{2E_i/m_e} \cos(\theta_j). \tag{8}$$

Note that here the velocity-space coordinate, $\mathbf{v}$, is not to be confused with the bulk velocity, $\mathbf{U}_e \equiv \frac{1}{n_e} \int \mathbf{v} f_e \mathrm{d}^3 v$ and that the minus signs are needed to flip the bin look direction to the actual plasma velocity direction. In this manuscript, we refer to $\partial f_e/\partial x$, $\partial f_e/\partial y$, $\partial f_e/\partial z$, and $\mathbf{v} \cdot \nabla f_e$, as "$\nabla f_e$ distributions." Each of these ∇f_e distributions can be visualized in the same manner used to show slices of the usual distribution function f_e.
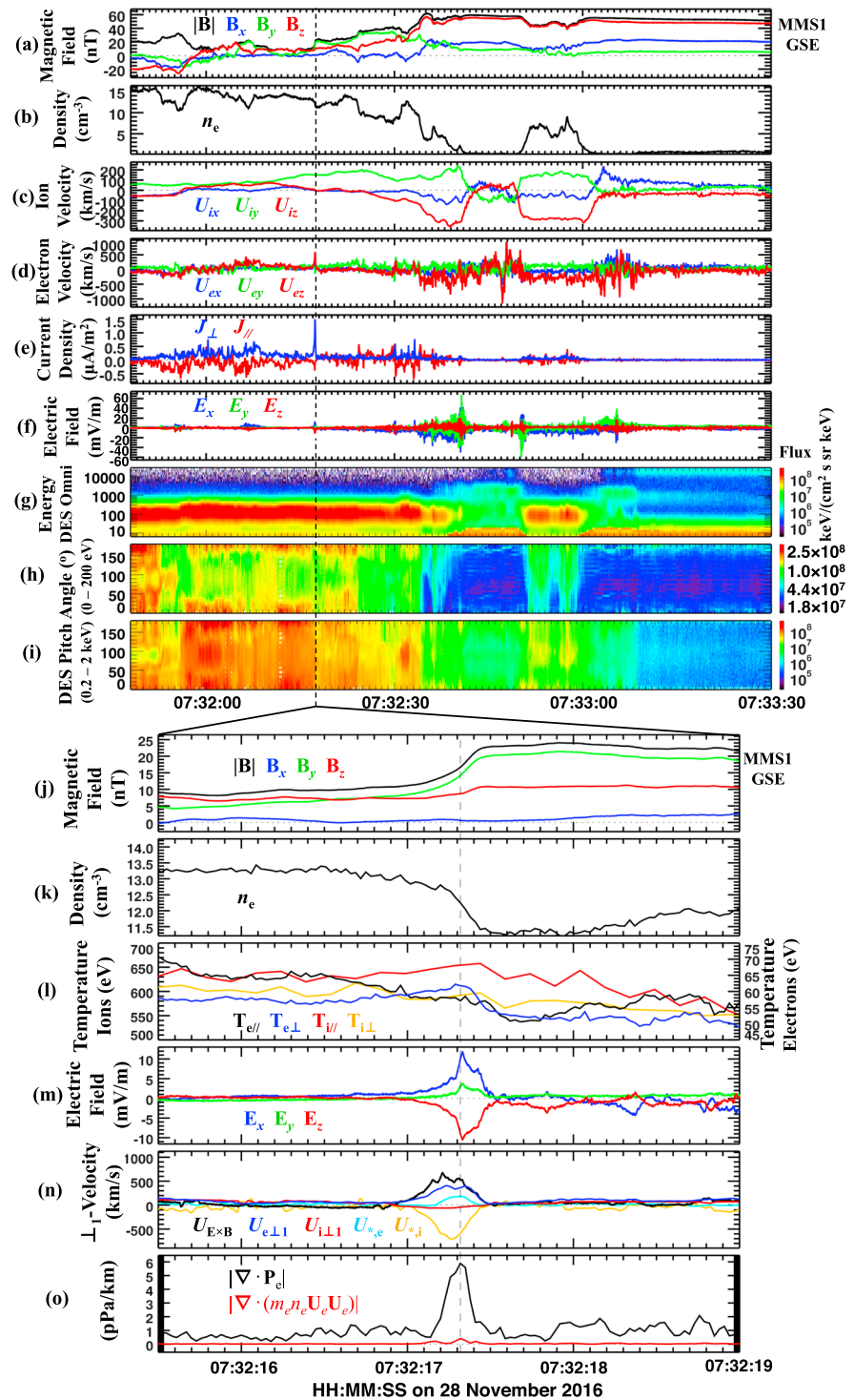
Figure 1. A thin (<10 d_e), strong ($J > 1\mu A/m^2$), isolated, perpendicular ($J_\perp > J_{\parallel}$), current sheet supported by electron flows captured by MMS in the vicinity of the magnetopause on 28 November 2016. The top panels present roughly 2 min of burst data showing the plasma context surrounding the current sheet as MMS transitioned from magnetosheath to magnetospheric plasma conditions: (a) magnetic field in GSE, (b) electron density, (c) ion velocity, (d) electron velocity, (e) perpendicular and parallel current density, (f) electric field, (g) DES omnidirectional electron energy spectrogram, and (h, i) low- and middle-energy electron pitch angle spectrograms. The bottom panels show a roughly 3-s zoom-in view of the current layer: (j) magnetic field (GSE), (k) electron density, (l) ion and electron temperatures, (m) electric field, (n) $\perp_1$ component of relevant velocities, and (o) comparison between the magnitudes of the electron pressure divergence and electron inertial term. MMS = Magnetospheric Multiscale; GSE = Geocentric Solar Ecliptic; DES = Dual Electron Spectrometer.

3. Electron-Scale Current Sheet Observations

A two-min overview of the high-resolution burst data interval from MMS 1 containing the first thin current sheet is shown in Figure 1 (top panels), with a 3.5-s zoom included below (bottom panels). The strong ($J_\perp \approx$ 1.5 μA/m^2) and otherwise isolated perpendicular current feature (Figure 1e, blue trace) stands out notably near 07:32:17 UT. This narrow current layer passes over the spacecraft in about 0.3 s. Moving forward in time, the current density structure matches the electron velocity profile and coincides with an increase in the magnetic field magnitude (mostly in the B_y component; see Figures 1a and 1j), a dip in the density (n_e goes from nearly 13.5 to 11.5 cm^{-3}; see Figures 1b and 1k), and enhancement of the electric field up to about 15 mV/m (Figures 1f and 1m). The electron temperature decreases slightly from about 60 to 50 eV (Figure 1l). Throughout the thin current layer, the ion velocity is steady at about $U_{iy} \approx$ 150 km/s (Figure 1c). The electron energy spectrogram (Figure 1g) also shows little variation during the few seconds surrounding this event, which appears to be embedded in the downstream MSH exhaust region far from the X-line of the diffusion region. On either side of the current layer, the electron low- (0 to 200 eV) and middle- (0.2 to 2 keV) energy pitch angle distributions (Figures 1h and 1i) show field-aligned and counterstreaming electron populations, which may be associated with electron trapping and reflection mechanisms associated with the far exhaust (e.g., Shuster et al., 2014; Wang et al., 2016).

During the interval from 07:32:00 to 07:33:10 UT, MMS transitions from high-density MSH plasma to low-density magnetospheric (MSP) conditions. From 07:32:40 to 07:33:00 UT, the electron energy spectrogram shows mixing of the MSH and MSP plasmas during enhanced and sheared ion flows with $U_{iz} <$ −300 km/s, which is indicative of a reconnection site northward of the spacecraft. The MSH-side separatrix is likely found near the time where the magnetic field B_z changes its sign almost a minute earlier around 07:31:57 UT. The thin current layer is found in the nonturbulent, intermediary region between the B_z sign change and the large density gradient, rather than at the separatrix or in the EDR. The two other thin current sheet events occur in similar fashion as MMS transitions from MSH to MSP plasma conditions. In each case, MMS observes strong, sheared ion flows on the MSP-side of the perpendicular current spike, which stands out among locally steady MSH conditions and coincides with localized gradients in |**B**| and n.

Ignoring inertial terms, the bulk perpendicular velocity of ions and electrons can be written as a sum of $\mathbf{E} \times \mathbf{B}$ and diamagnetic drifts

$$\mathbf{U}_{i\perp} = \frac{\mathbf{E} \times \mathbf{B}}{B^2} - \frac{(\nabla \cdot \mathbf{P}_i) \times \mathbf{B}}{enB^2} = \mathbf{U}_{E \times B} + \mathbf{U}_{*,i}, \tag{9}$$

$$\mathbf{U}_{e\perp} = \frac{\mathbf{E} \times \mathbf{B}}{B^2} + \frac{(\nabla \cdot \mathbf{P}_e) \times \mathbf{B}}{enB^2} = \mathbf{U}_{E \times B} + \mathbf{U}_{*,e}, \tag{10}$$

where $\mathbf{U}_{E \times B}$ is the $\mathbf{E} \times \mathbf{B}$ drift velocity and $\mathbf{U}_{*,j} = -(\nabla \cdot \mathbf{P}_j) \times \mathbf{B}/(q_j n_j B^2)$ is the species-dependent diamagnetic drift velocity (e.g., Swisdak et al., 2003). The dominant contribution to the perpendicular electron velocity $U_{e\perp 1}$ is provided by $\mathbf{E} \times \mathbf{B}$ drifting electrons, whereas the effect of $\mathbf{E} \times \mathbf{B}$ for ions is balanced by $\mathbf{U}_{*,i}$ resulting in $U_{i\perp 1} \approx 0$, where the $\perp_1$ direction points along $(-\mathbf{U}_e \times \mathbf{B}) \times \mathbf{B}$ (approximately the $\mathbf{E} \times \mathbf{B}$ direction) and the $\perp_2$ direction points along $-\mathbf{U}_e \times \mathbf{B}$ (roughly along $\mathbf{E}$ and ∇n_e). To obtain $\mathbf{U}_{*,i}$ at the electron time resolution, we assume quasineutrality ($n_i \approx n_e$), interpolate the ion temperature to the electron temporal resolution, and neglect the divergence of the ion temperature ($\nabla \cdot \mathbf{T}_i \approx 0$), which yields $\nabla \cdot \mathbf{P}_i \approx \mathbf{T}_i \cdot \nabla n_e$. As a test of the reliability of the multispacecraft spatial gradient determination for these events, we compare $\mathbf{J}_{\text{FGM}} \times \mathbf{B}$ to $\nabla \cdot \mathbf{P}$, where $\mathbf{J}_{\text{FGM}}$ is computed using the fluxgate magnetometer (FGM) data (Russell et al., 2016) via the curlometer method: $\mathbf{J}_{\text{FGM}} \approx \nabla \times \mathbf{B}/\mu_0$ (Dunlop et al., 1988), and $\nabla \cdot \mathbf{P} = \nabla \cdot \mathbf{P}_i + \nabla \cdot \mathbf{P}_e$ is computed using FPI data.

Figure 1n illustrates how for these events the ion diamagnetic drift $\mathbf{U}_{*,i}$ (gold trace), computed using the approximation $\nabla \cdot \mathbf{P}_i \approx \mathbf{T}_i \cdot \nabla n_e$, mostly balances with the $\mathbf{E} \times \mathbf{B}$ drift averaged over the four spacecraft (black trace), resulting in a small average $U_{i\perp}$ (red trace). Because T_i is roughly an order of magnitude larger than T_e, the ion pressure provides the dominant contribution to the force balance, consistent with Hesse et al. (2008) and Pritchett (2008). Since $U_{e\perp} \gg U_{i\perp}$, we have $\mathbf{J}_\perp \approx -en\mathbf{U}_{e\perp}$. This, along with $\mathbf{U}_{e\perp} \approx \mathbf{U}_{E \times B}$ and $\mathbf{U}_{*,i} \approx -\mathbf{U}_{E \times B}$, implies $\mathbf{J}_\perp \approx en\mathbf{U}_{*,i}$, and thus, we expect $\mathbf{J} \times \mathbf{B} \approx \nabla \cdot \mathbf{P}_i$. Similar results were found by Graham et al. (2016) in the ion diffusion region, though the events of our study are in the exhaust region far from typical diffusion region signatures.
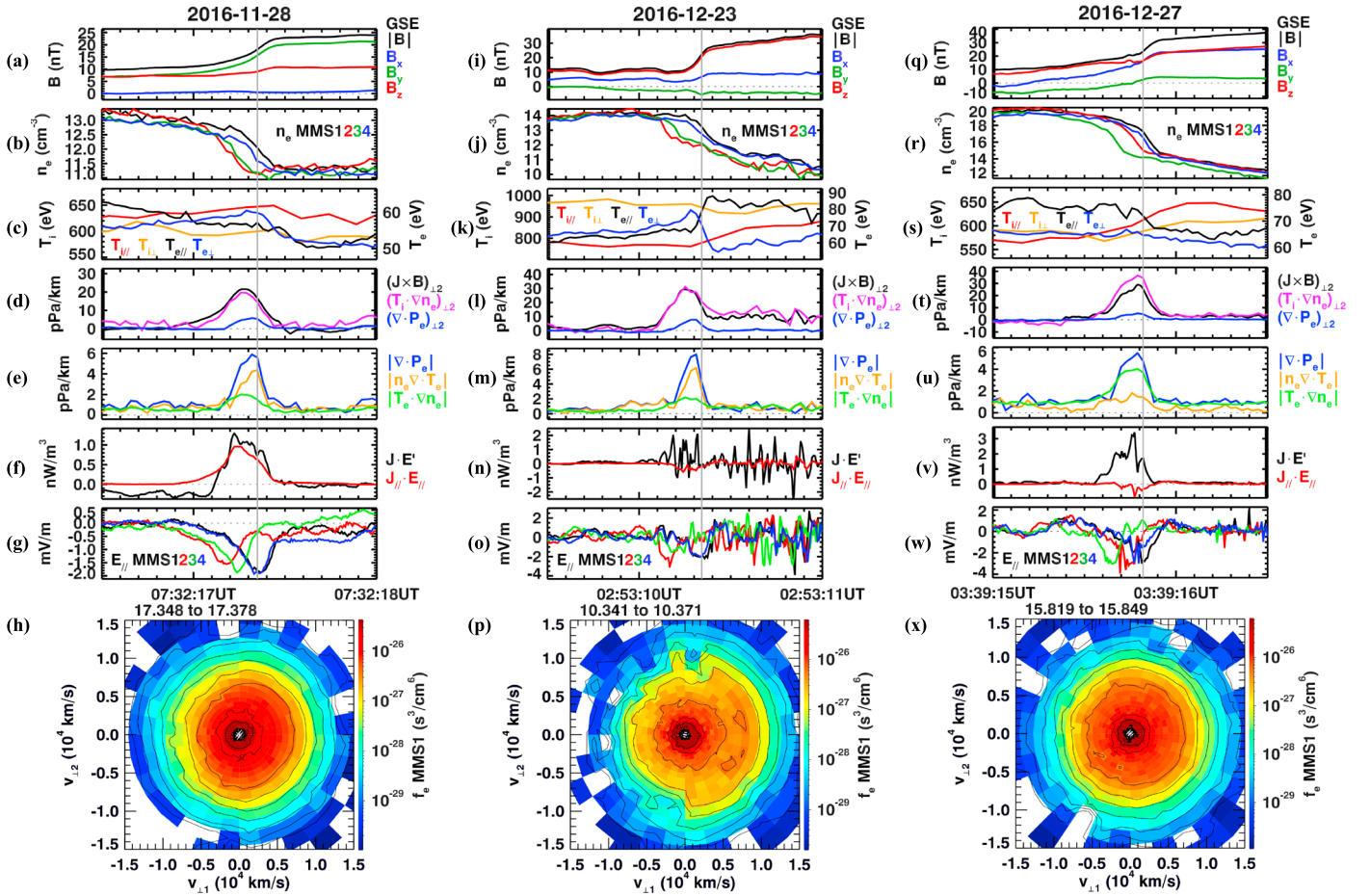
Figure 2. Three electron-scale current sheets detected by MMS. All quantities are averaged over the four spacecraft, unless stated. (a, i, q) Magnetic field in GSE measured by MMS 1; (b, j, r) Four spacecraft electron densities, (c, k, s) ion and electron temperatures measured by MMS 1; (d, l, t) $\perp_2$ components of $\mathbf{J} \times \mathbf{B}$ (black), $\mathbf{T}_i \cdot \nabla n_e$ (magenta), and $\nabla \cdot \mathbf{P}_e$ (blue), where $\mathbf{J} = \nabla \times \mathbf{B}/\mu_0$ is crossed with the average magnetic field; (e, m, u) decomposition of $\nabla \cdot \mathbf{P}_e$ into $n_e \nabla \cdot \mathbf{T}_e$ (orange) and $\mathbf{T}_e \cdot \nabla n_e$ (green); (f, n, v) energy conversion as measured by $\mathbf{J} \cdot \mathbf{E}'$ and $J_{\|}E_{\|}$; (g, o, w) four spacecraft parallel electric fields; and (h, p, x) $v_{\perp 1}$-$v_{\perp 2}$ slices of f_e as measured by MMS1 taken from the time indicated by the vertical gray line in the panels above for each event. The 30-ms time intervals over which the distributions were accumulated are displayed in seconds above each distribution panel. MMS = Magnetospheric Multiscale; GSE = Geocentric Solar Ecliptic.

The $\nabla \cdot \mathbf{P}_e$ associated with each current layer is directed mainly along the $\perp_2$ direction, which is roughly in the same direction as ∇n_e. The 1.5-s intervals shown in Figure 2 provide a side-by-side comparison of the bulk and kinetic properties of the three thin current sheets. The top three panels for each event (Figures 2a–2c, 2i–2k, and 2q–2s) show the magnetic field, four-spacecraft density, and ion and electron temperatures. The fourth panels (Figures 2d, 2l, and 2t) show the $\perp_2$ component of the force balance between $\mathbf{J} \times \mathbf{B}$ as measured by FGM compared to $\nabla \cdot \mathbf{P} \approx \mathbf{T}_i \cdot \nabla n_e$ as measured by FPI. There is reasonable agreement with $\mathbf{J} \times \mathbf{B}$ (compare black and magenta traces), aside from some offsets on the order of a few picopascals per kilometer, which gives confidence in using the gradient approximation. The fifth panels (Figures 2e, 2m, and 2u) show that for Events 1, 2, and 3, $|\nabla \cdot \mathbf{P}_e|$ contributes 6, 8, and 5 pPa/km, which is about 30%, 27%, and 20% of $|\mathbf{J} \times \mathbf{B}|$, respectively. Decomposing the electron pressure divergence into its density gradient and temperature divergence contributions, we find that for the first two events $n_e \nabla \cdot \mathbf{T}_e$ is larger, whereas for the third event $\mathbf{T}_e \cdot \nabla n_e$ is dominant. We neglect the electron inertial terms since for Events 1, 2, and 3, $|\nabla \cdot (m_e n_e \mathbf{U}_e \mathbf{U}_e)|$ is about 50, 10, and 25 times smaller than $\nabla \cdot \mathbf{P}_e$, respectively (e.g., Figure 1o).

A small yet finite parallel electric field $E_{\|}$ and parallel current $J_{\|}$ are also associated with these events. Energy conversion from fields to particles exists within the presented current layers, as indicated by $\mathbf{J} \cdot \mathbf{E}' = \mathbf{J} \cdot (\mathbf{E} + \mathbf{U}_e \times \mathbf{B}) > 0$, which is not directly associated with a diffusion region X-line (see Figures 2f, 2n, and 2v). For the first event, $\mathbf{J} \cdot \mathbf{E}'$ results predominantly from $J_{\|}E_{\|}$ with a small (≈ -2 mV/m) yet coherent $E_{\|}$ feature observed by each of the four spacecraft (Figure 2g), which is above the electric field probes' instrument error
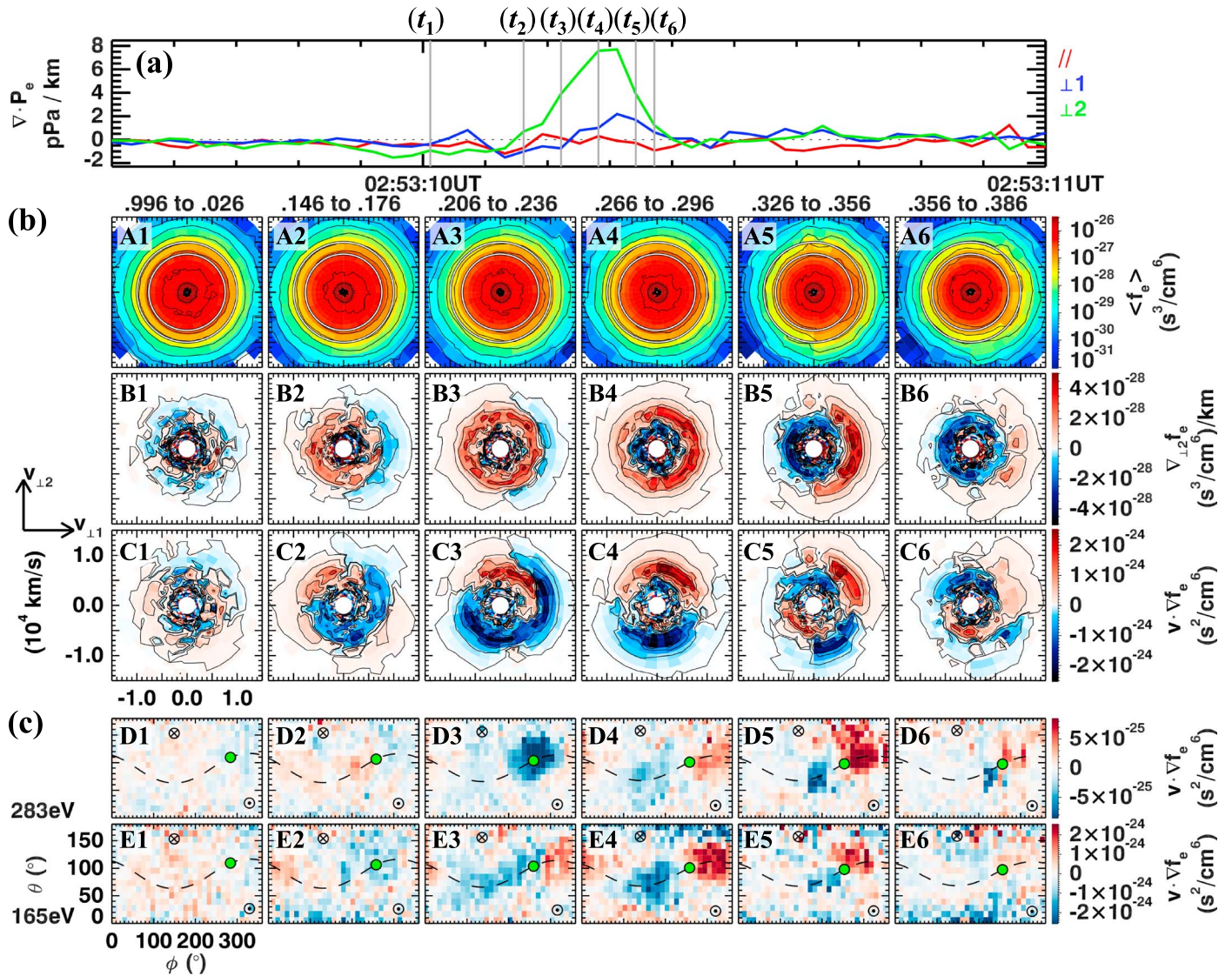
Figure 3. Visualization of electron phase space density gradients and terms in the Vlasov equation for the thin current sheet observed on 23 December 2016 (Event 2). (a) $\nabla \cdot \mathbf{P}_e$ in field-aligned coordinates. (b) $v_{\perp 1}$-$v_{\perp 2}$ velocity space slices of $<f_e>$ (Row A), $\nabla_{\perp 2} f_e$ (Row B), and $\mathbf{v} \cdot \nabla f_e$ (Row C). (c) Angle-angle (θ-ϕ) space visualizations of $\mathbf{v} \cdot \nabla f_e$ at 283 eV (Row D) and 165 eV (Row E). The six columns of distributions correspond to the 30-ms time intervals t_1 through t_6 written above the distributions in Row A and indicated by the vertical lines in (a). In Rows D and E, the green circle indicates the $\mathbf{E} \times \mathbf{B}$ direction, and directions parallel and antiparallel to the magnetic field are denoted by the black dot and cross symbols, respectively.

threshold (about ± 1 mV/m for this interval). The second event exhibits oscillating $\mathbf{J} \cdot \mathbf{E}'$ signatures mainly contributed by the perpendicular component $J_\perp E_\perp$. The oscillations are associated with finer structures of the electric field that may be due to wave instabilities. The third event features a roughly 3 nW/m³ $\mathbf{J} \cdot \mathbf{E}'$ feature dominated by $J_\perp E_\perp$, while coherent $E_\parallel$ signatures are present for all four spacecraft.

A slice of the electron velocity distribution in $v_{\perp 1}$-$v_{\perp 2}$ space for each event (Figures 2h, 2p, and 2x) shows the kinetic structure of electrons within the thin current sheet. For Events 1 and 3, the electron distribution shows a shift in the $v_{\perp 1}$ direction, while Event 2 exhibits a distinct crescent-shaped electron population centered at roughly 0.7×10^4 km/s along the $v_{\perp 1}$ direction. The crescent feature at this electron-scale boundary layer can be explained by finite gyroradius and diamagnetic effects of the magnetized electrons, rather than unmagnetized electrons that would be associated with an EDR (Egedal et al., 2016; Rager et al., 2018). The local nongyrotropy of the electrons in the current layer and the region of anisotropic electrons exhibiting $T_{e\parallel} > T_{e\perp}$ may be the source of the wave instabilities found on the MSP-side of the layer (e.g., Graham et al., 2017; Le et al., 2017).

4. Kinetic Origins of the Electron Pressure Divergence: Insight From the Vlasov Equation

Velocity space visualizations of ∇f_e offer a kinetic perspective into which electron populations contribute to the bulk electron pressure divergence $\nabla \cdot \mathbf{P}_e$, analogously to how visualizations of the distribution function f_e offer a kinetic perspective into the electron populations contributing to the bulk electron velocity $\mathbf{U}_e$. Figure 3b shows a series of $v_{\perp 1}$-$v_{\perp 2}$ velocity space slices of $<f_e> = \left(f_e^{\mathrm{MMS1}} + f_e^{\mathrm{MMS2}} + f_e^{\mathrm{MMS3}} + f_e^{\mathrm{MMS4}} \right)/4$ (row A), $\nabla_{\perp 2} f_e$ (row B), and $\mathbf{v} \cdot \nabla f_e$ (row C) sampling the current layer supported by the electron crescent distribution (Event 2), taken at six times labeled (t_1) through (t_6) indicated by the vertical lines in the top panel showing the $\nabla \cdot \mathbf{P}_e$ vector in field-aligned coordinates (Figure 3a). The last two rows show the energy dependence of $\mathbf{v} \cdot \nabla f_e$ in full-sky angle-angle (θ-ϕ) space for 283 eV (Row D) and 165 eV (Row E). Thin white rings at the velocities corresponding to these two energies are displayed on top of the $<f_e>$ distributions (in Row A) for reference.

Intricate and coherent structures in the $\nabla_{\perp 2} f_e$ and $\mathbf{v} \cdot \nabla f_e$ distributions develop toward the maximum $(\nabla \cdot \mathbf{P}_e)_{\perp 2}$ within the current layer (green trace in Figure 3a). In particular, semicircular and crescent-shaped features of opposite polarity form in the $\nabla_{\perp 2} f_e$ distributions (Row B). Since the $\perp_2$ direction points roughly along the density gradient ∇n_e direction, we can interpret the $\nabla_{\perp 2} f_e$ measurements as follows: $\nabla_{\perp 2} f_e > 0$ means that if we move spatially along the ∇n_e direction, the electron phase space density f_e will *increase* for that portion of velocity space. Likewise, $\nabla_{\perp 2} f_e < 0$ indicates that along the ∇n_e direction, f_e will *decrease*. Initially outside the current layer (distribution B1), the $\nabla_{\perp 2} f_e$ distribution lacks significant structure. Beginning with distribution B2 and moving to B6, a crescent structure on the $+v_{\perp 1}$ side of the slice (centered near $v_{\perp 1} = 10^4$ km/s) develops and transitions from $\nabla_{\perp 2} f_e < 0$ (blue) to $\nabla_{\perp 2} f_e > 0$ (red) throughout the $\nabla \cdot \mathbf{P}_e$ layer. From distribution B2 to B3, the gyrophase extent of the negative $\nabla_{\perp 2} f_e$ crescent region diminishes. At the $(\nabla \cdot \mathbf{P}_e)_{\perp 2}$ maximum near 02:53:10.300 UT, distribution B4 exhibits a ring-like feature of positive $\nabla_{\perp 2} f_e > 0$. On the other side of the current layer in distribution B5, $\nabla_{\perp 2} f_e$ for the crescent has changed sign and is now positive (red). Beyond distribution B6, the crescent-shaped region fades away and begins to resemble the type of signal outside of the current layer (similar to distribution B1). At its maximum, $\nabla_{\perp 2} f_e$ within the crescent region reaches about 5×10^{-28} (s^3/cm^6)/km. From B2 to B6, the sign of $\nabla_{\perp 2} f_e$ for lower velocities (roughly $|\mathbf{v}| < 0.5 \times 10^4$ km/s) goes from positive to negative, always opposite of the sign of $\nabla_{\perp 2} f_e$ in the higher-velocity crescent region. The evolution of $\nabla_{\perp 2} f_e$ distributions for Events 1 and 3 exhibit qualitatively similar structures to those shown for Event 2 in Figure 3, though for Event 3 the crescent structures are less pronounced.

The alternating sign of the crescent structure in $\nabla_{\perp 2} f_e$ can be interpreted intuitively. On the high-density side of the current layer, the $\perp_2$ direction (roughly along ∇n_e) points away from the current layer, whereas on the low-density side, the $\perp_2$ direction points toward the peak current region. The current layer is supported by a crescent-shaped population of electrons (Figure 3p). Thus, on the low-density side of the layer, the positive $\nabla_{\perp 2} f_e$ gradient (red crescent) indicates that the phase space density of these crescent electrons is *increasing* when moving toward the center of the layer; on the high-density side of the current layer, the negative $\nabla_{\perp 2} f_e$ gradient (blue crescent) indicates that the phase space density of the crescent electrons is *decreasing* when moving away from the center of the layer. This is consistent with expectation, since we would expect to see an increased number of higher-velocity crescent electrons as we enter the layer and approach the region of peak current and to see a decreased number of crescent electrons as we exit the layer. For the lower energies, the situation is reversed: we expect fewer low-energy electrons as we move into the current layer supported by strong electron flows, and more low-energy electrons upon exiting the layer, as observed.

Since $\nabla_{\perp 2} f_e$ is the dominant component of ∇f_e, the approximation $\mathbf{v} \cdot \nabla f_e \approx v_{\perp 2} \nabla_{\perp 2} f_e$ helps to explain features of the $\mathbf{v} \cdot \nabla f_e$ distributions. For example, multiplying distribution B5 by $v_{\perp 2}$ preserves the sign of the upper half of distribution B5 (where $v_{\perp 2} > 0$) while reversing the sign of the lower half (where $v_{\perp 2} < 0$), which explains the resulting quadrupolar structure of $\mathbf{v} \cdot \nabla f_e$ in distribution C5. The same heuristic approach explains how the bipolar structure of $\mathbf{v} \cdot \nabla f_e$ in distribution C4 arises from the circular structure of $\nabla_{\perp 2} f_e$ in distribution B4. The $\mathbf{v} \cdot \nabla f_e$ structures in C2 and C3 are more complicated because of a nonnegligible $v_{\perp 1} \nabla_{\perp 1} f_e$ term. Ultimately, $\nabla \cdot \mathbf{P}_e$ originates from the velocity-weighted integral (over all angles and energies) of the $\mathbf{v} \cdot \nabla f_e$ distributions (equation (2)). This explains why t_4 is the time of maximum $(\nabla \cdot \mathbf{P}_e)_{\perp 2} \propto v_{\perp 2}(\mathbf{v} \cdot \nabla f_e)$: again, multiplying the $\mathbf{v} \cdot \nabla f_e$ structure in distribution C4 by $v_{\perp 2}$ reverses the sign of $\mathbf{v} \cdot \nabla f_e$ in the lower ($v_{\perp 2} < 0$) half of the distribution, so that both peaks contribute positively to the $(\nabla \cdot \mathbf{P}_e)_{\perp 2}$ calculation. Similar visual

analysis of structures in $\nabla_{\perp 1} f_e$ (data not shown) explains the slight bipolar $(\nabla \cdot \mathbf{P}_e)_{\perp 1}$ feature in Figure 3a (blue trace). There are no coherent structures in $\nabla_{\parallel} f_e$, which is why $(\nabla \cdot \mathbf{P}_e)_{\parallel}$ is small throughout the layer (red trace in Figure 3a).

The full-sky distributions in angle-angle space (Rows D and E) offer an alternate perspective into the $\mathbf{v} \cdot \nabla f_e$ distribution structures. For reference, the directions parallel and antiparallel to the magnetic field are indicated by the black dot and cross symbols, respectively. The black dashed curve covers bins with 90° pitch angle, and the green dot along this curve denotes the $\mathbf{E} \times \mathbf{B}$ direction (approximately the $\perp_1$ direction). The enhancement of $\mathbf{v} \cdot \nabla f_e$ centered on the $\mathbf{E} \times \mathbf{B}$ direction in distribution D3 results from a significant contribution of $v_{\perp 1} \nabla_{\perp 1} f_e$ to the total $\mathbf{v} \cdot \nabla f_e$, which explains the asymmetry of distribution C3, as noted above. The coherent bipolar signature in $\mathbf{v} \cdot \nabla f_e$ first appears at lower energies (e.g., distribution E4) and then moves to higher energies (e.g., distribution D5) during the time interval from t_2 to t_6. This feature corresponding to the crescent-shaped regions in the distributions above is observed in the angle-angle maps for six consecutive energy steps (two of which are shown), covering an energy range of 126 to 485 eV (about 6,700 to 13,100 km/s). These visualizations thus allow us to isolate which energy electrons directly contribute to $\nabla \cdot \mathbf{P}_e$ and to quantify their distribution throughout velocity space.

To assess the uncertainties in the ∇f_e measurements, we implemented a Monte Carlo resampling technique. Using the provided standard deviations of f_e for the four spacecraft (see Gershman et al., 2015, and references therein), we generated a set of 100 statistically equivalent f_e distributions from which we calculated a corresponding sample of ∇f_e and $\mathbf{v} \cdot \nabla f_e$ distributions. The reported features of the ∇f_e and $\mathbf{v} \cdot \nabla f_e$ distributions clearly persist for all 100 resampled distributions. The standard deviations of the ∇f_e and $\mathbf{v} \cdot \nabla f_e$ measurements for this sample are comparable to the error in f_e, which is on the order of 10% of the measurement magnitude.

5. Discussion and Conclusions

We report three electron-scale current sheets observed by MMS in the vicinity of the dayside magnetopause. From multispacecraft timing analysis, the width of the current layers is on the order of 5 to 15 d_e. Without significant reversal or rotation of the magnetic field, these current structures are likely embedded within the MSH exhaust far downstream from the reconnection diffusion region. Since there is no apparent reversal in the electron jets and the current structures appear isolated from any highly turbulent regions, they also do not appear to be undergoing "electron-only" reconnection as recently discussed by Phan et al. (2018). The strong perpendicular electron flows develop from $\mathbf{E} \times \mathbf{B}$ drifting electrons, while the effect of $\mathbf{E} \times \mathbf{B}$ on the ions is negated by their diamagnetic drift due to the substantial $\nabla \cdot \mathbf{P}_i$, which provides the dominant contribution to balance the $\mathbf{J} \times \mathbf{B}$ force within the current layers, consistent with previous studies (e.g., Hesse et al., 2008; Pritchett, 2008; Graham et al., 2016). In addition, each of these thin current sheets supports nonideal energy conversion mechanisms based on positive $\mathbf{J} \cdot \mathbf{E}'$ measured within each layer. These results provide observational constraints to aid in the development of current sheet models which satisfy exact Vlasov equilibrium (e.g., Yoon & Lui, 2005). One of the current sheets (Event 2) is supported by an electron crescent distribution, which is expected to form at electron-scale boundaries due to finite gyroradius effects (e.g., Egedal et al., 2016). Nevertheless, the sharp kinetic-scale density gradient and local nongyrotropy of the distribution may be the source of the wave instabilities on the MSP-side of the layer (e.g., Graham et al., 2017). The thin current sheets reported here may correspond to the electron inertial scale current sheet filaments that form in the outflow region and mixing layers predicted by 3-D particle-in-cell simulations (Daughton et al., 2014; Le et al., 2017), which would suggest that these currents can account for a substantial amount of energy converted from fields to particles outside of the separatrix and diffusion regions.

MMS measurements of electron phase space density gradients and the spatial gradient term in the Vlasov equation $\mathbf{v} \cdot \nabla f_e$ reveal kinetic structures that characterize the electron pressure divergence within these thin current sheets. A crescent-shaped region of negative $\nabla_{\perp 2} f_e$ develops entering the current layer, becomes a ring with $\nabla_{\perp 2} f_e > 0$ at the maximum $\nabla \cdot \mathbf{P}_e$, and then transitions to a positive $\nabla_{\perp 2} f_e$ crescent upon exiting the layer. Lower-energy electrons exhibit a reversal in polarity of $\nabla_{\perp 2} f_e$ that is opposite to that of the higher-velocity crescent. Thus, phase space density increases for higher energies and decreases for lower energies when moving toward the center of the current layer. These $\nabla_{\perp 2} f_e$ features give $\mathbf{v} \cdot \nabla f_e$ a quadrupolar structure in velocity space. In angle-angle space, corresponding bipolar signatures in $\mathbf{v} \cdot \nabla f_e$ centered around the $\mathbf{E} \times \mathbf{B} \, (\perp_1)$ direction range from 126 to 485 eV and are found to increase in energy over time.

The unprecedented spatiotemporal and velocity-space resolution of FPI enables measurement of electron phase space density gradients and terms of the Vlasov equation, which can provide insight into the fundamental kinetic structure of the electron pressure divergence that forms within the types of thin current layers considered here, as well as other fundamental electron-scale structures that develop throughout the Earth's magnetosphere. Our technique may be applied to ascertain the kinetic origins of the divergence of the nongyrotropic components of the pressure tensor believed to be responsible for sustaining the nonideal electric field necessary to fuel magnetic reconnection in the EDR (e.g, Hesse et al., 2011). Comparing spacecraft measurements of Vlasov equation terms acquired using ours and other recently proposed techniques (e.g., Klein & Howes, 2016) to predictions from recent kinetic simulations (e.g., Shuster et al., 2015; Shuster et al., 2017; Wang et al., 2016; Wang et al., 2018) is needed to deepen our knowledge of fundamental energy conversion and electron energization mechanisms.

References

Bessho, N., Chen, L.-J., & Hesse, M. (2016). Electron distribution functions in the diffusion region of asymmetric magnetic reconnection. *Geophysics Research Letter*, *43*, 1828–1836. https://doi.org/10.1002/2016GL067886

Burch, J. L., Torbert, R. B., Phan, T. D., Chen, L.-J., Moore, T. E., Ergun, R. E., et al. (2016). Electron-scale measurements of magnetic reconnection in space. *Science*, *352*, aaf2939. https://doi.org/10.1126/science.aaf2939

Califano, F., Manfredi, G., & Valentini, F. (2016). Special issue: The Vlasov equation, from space to laboratory plasmas. *Journal Plasma Physics*, *82*(6), 701820603. https://doi.org/10.1017/S002237781600115X

Chen, L.-J., Hesse, M., Wang, S., Gershman, D., Ergun, R., Pollock, C., et al. (2016). Electron energization and mixing observed by MMS in the vicinity of an electron diffusion region during magnetopause reconnection. *Geophysics Research Letter*, *43*, 6036–6043. https://doi.org/10.1002/2016GL069215

Chen, L.-J., Hesse, M., Wang, S., Gershman, D., Ergun, R. E., Burch, J., et al. (2017). Electron diffusion region during magnetopause reconnection with an intermediate guide field: Magnetospheric multiscale observations. *Journal Geophysics Research: Space Physics*, *122*, 5235–5246. https://doi.org/10.1002/2017JA024004

Daughton, W. (2002). Nonlinear dynamics of thin current sheets. *Physics Plasmas*, *9*(9), 3668–3678. https://doi.org/10.1063/1.1499118

Daughton, W., Nakamura, T. K. M., Karimabadi, H., Roytershteyn, V., & Loring, B. (2014). Computing the reconnection rate in turbulent kinetic layers by using electron mixing to identify topology. *Physics Plasmas*, *21*(5), 52307. https://doi.org/10.1063/1.4875730

Dunlop, M. W., Southwood, D. J., Glassmeier, K.-H., & Neubauer, F. M. (1988). Analysis of multipoint magnetometer data. *Advance Space Research*, *8*(9), 273–277. https://doi.org/10.1016/0273-1177(88)90141-X

Egedal, J., Le, A., Daughton, W., Wetherton, B., Cassak, P. A., Chen, L.-J., et al. (2016). Spacecraft observations and analytic theory of crescent-shaped electron distributions in asymmetric magnetic reconnection. *Physical Review Letters*, *117*, 185101. https://doi.org/10.1103/PhysRevLett.117.185101

Eriksson, S., Wilder, F. D., Ergun, R. E., Schwartz, S. J., Cassak, P. A., Burch, J. L., et al. (2016). Magnetospheric multiscale observations of the electron diffusion region of large guide field magnetic reconnection. *Physical Review Letters*, *117*, 15001. https://doi.org/10.1103/PhysRevLett.117.015001

Genestreti, K. J., Burch, J. L., Cassak, P. A., Torbert, R. B., Ergun, R. E., Varsani, A., et al. (2017). The effect of a guide field on local energy conversion during asymmetric magnetic reconnection: MMS observations. *Journal of Geophysical Research: Space Physics*, *122*, 353. https://doi.org/10.1002/2017JA024247

Genestreti, K. J., Varsani, A., Burch, J. L., Cassak, P. A., Torbert, R. B., Nakamura, R., et al. (2018). MMS observation of asymmetric reconnection supported by 3-D electron pressure divergence. *Journal of Geophysical Research: Space Physics*, *123*, 1806–1821. https://doi.org/10.1002/2017JA025019

Gershman, D. J., Dorelli, J. C., Viñas, A. F., & Pollock, C. J. (2015). The calculation of moment uncertainties from velocity distribution functions with random errors. *Journal of Geophysical Research: Space Physics*, *120*, 6633–6645. https://doi.org/10.1002/2014JA020775

Gershman, D. J., F-Viñas, A., Dorelli, J. C., Dorelli, J. C., Boardsen, S. A., Avanov, L. A., et al. (2017). Wave-particle energy exchange directly observed in a kinetic Alfvén-branch wave. *Nature Communications*, *8*, 14719. https://doi.org/10.1038/ncomms14719

Graham, D. B., Khotyaintsev, Y. V., Norgren, C., Vaivads, A., André, M., Lindqvist, P.-A., et al. (2016). Electron currents and heating in the ion diffusion region of asymmetric reconnection. *Geophysical Research Letters*, *43*, 4691–4700. https://doi.org/10.1002/2016GL068613

Graham, D. B., Khotyaintsev, Y. V., Vaivads, A., Norgren, C., André, M., Webster, J. M., et al. (2017). Instability of agyrotropic electron beams near the electron diffusion region. *Physical Review Letters*, *119*, 25101. https://doi.org/10.1103/PhysRevLett.119.025101

Gurnett, D. A., & Bhattacharjee, A. (2005). *Introduction to plasma physics with space and laboratory applications*. New York: Cambridge University Press. https://doi.org/10.1017/CBO9780511809125

Harris, E. G. (1962). On a plasma sheath separating regions of oppositely directed magnetic field. *Nuovo Cimento*, *23*(1), 115–121. https://doi.org/10.1007/BF02733547

Harvey, C. C. (1998). Spatial gradients and the volumetric tensor. In G. Paschmann & P. W. Daly (Eds.), *Analysis methods for multi-spacecraft data*, ISSI Scientific Reports Series (pp. 307–322). Noordwijk, Netherlands: ISSI/ESA.

Hesse, M., Neukirch, T., Schindler, K., Kuznetsova, M., & Zenitani, S. (2011). The diffusion region in collisionless magnetic reconnection. *Space Science Reviews*, *160*(1), 3–23. https://doi.org/10.1007/s11214-010-9740-1

Hesse, M., Zenitani, S., & Klimas, A. (2008). The structure of the electron outflow jet in collisionless magnetic reconnection. *Physics Plasmas*, *15*(11), 112102. https://doi.org/10.1063/1.3006341

Klein, K. G., & Howes, G. G. (2016). Measuring collisionless damping in heliospheric plasmas using field-particle correlations. *Astrophysics Jounal Letters*, *826*(2), L30. https://doi.org/10.3847/2041-8205/826/2/l30

Le, A., Daughton, W., Chen, L.-J., & Egedal, J. (2017). Enhanced electron mixing and heating in 3-D asymmetric reconnection at the Earth's magnetopause. *Geophysics Research Letters*, *44*, 2096–2104. https://doi.org/10.1002/2017GL072522

Nicholson, D. R. (1983). *Introduction to plasma theory*. New York: Wiley.

Norgren, C., Graham, D. B., Khotyaintsev, Y. V., André, M., Vaivads, A., Chen, L.-J., et al. (2016). Finite gyroradius effects in the electron outflow of asymmetric magnetic reconnection. *Geophysics Research Letters*, *43*, 6724–6733. https://doi.org/10.1002/2016GL069205

Phan, T. D., Eastwood, J. P., Cassak, P. A., M. Øieroset, M., Gosling, J. T., Gershman, D. J., et al. (2016). MMS observations of electron-scale filamentary currents in the reconnection exhaust and near the X line. *Geophysics Research Letters*, *43*, 6060–6069. https://doi.org/10.1002/2016GL069212

Phan, T. D., Eastwood, J. P., Shay, M. A., Drake, J. F., Ö. Sonnerup, B. U., Fujimoto, M., et al. (2018). Electron magnetic reconnection without ion coupling in Earth's turbulent magnetosheath. *Nature*, *557*, 202–206. https://doi.org/10.1038/s41586-018-0091-5

Pollock, C., Moore, T., Jacques, A., Burch, J., Gliese, U., Saito, Y., et al. (2016). Fast plasma investigation for magnetospheric multiscale. *Space Science Reviews*, *199*(1), 331–406. https://doi.org/10.1007/s11214-016-0245-4

Priest, E. R. (1976). Current sheet models of solar flares. *Solar Physics*, *47*(1), 41–75. https://doi.org/10.1007/BF00152244

Pritchett, P. L. (2008). Collisionless magnetic reconnection in an asymmetric current sheet. *Journal Geophysics Research*, *113*, A06210. https://doi.org/10.1029/2007JA012930

Rager, A. C., Dorelli, J. C., Gershman, D. J., Uritsky, V., Avanov, L. A., Torbert, R. B., et al. (2018). Electron crescent distributions as a manifestation of diamagnetic drift in an electron-scale current sheet: Magnetospheric multiscale observations using new 7.5 ms fast plasma investigation moments. *Geophysics Research Letters*, *45*, 578–584. https://doi.org/10.1002/2017GL076260

Russell, C. T., Anderson, B. J., Baumjohann, W., Bromund, K. R., Dearborn, D., Fischer, D., et al. (2016). The magnetospheric multiscale magnetometers. *Space Science Reviews*, *199*(1), 189–256. https://doi.org/10.1007/s11214-014-0057-3

Shuster, J. R., Argall, M. R., Torbert, R. B., Chen, L.-J., Farrugia, C. J., Alm, L., et al. (2017). Hodographic approach for determining spacecraft trajectories through magnetic reconnection diffusion regions. *Geophysical Research Letters*, *44*, 1625–1633. https://doi.org/10.1002/2017GL072570

Shuster, J. R., Chen, L.-J., Daughton, W. S., Lee, L. C., Lee, K. H., Bessho, N., et al. (2014). Highly structured electron anisotropy in collisionless reconnection exhausts. *Geophysics Research Letters*, *41*, 5389–5395. https://doi.org/10.1002/2014GL060608

Shuster, J. R., Chen, L.-J., Hesse, M., Argall, M. R., Daughton, W., Torbert, R. B., & Bessho, N. (2015). Spatiotemporal evolution of electron characteristics in the electron diffusion region of magnetic reconnection: Implications for acceleration and heating. *Geophysics Research Letters*, *42*, 2586–2593. https://doi.org/10.1002/2015GL063601

Shuster, J. R., Gershman, D., Dorelli, J., Shan Wang S., Bessho, N., Chen, L.-J., et al. (2019). Resolving terms of Vlasov's equation with MMS. *Earth and Space Science Open Archive*. https://doi.org/10.1002/essoar.10500727.1

Sundkvist, D., Retinò, A., Vaivads, A., & Bale, S. D. (2007). Dissipation in turbulent plasma due to reconnection in thin current sheets. *Physical Review Letters*, *99*, 25004. https://doi.org/10.1103/PhysRevLett.99.025004

Swisdak, M., Rogers, B. N., Drake, J. F., & Shay, M. A. (2003). Diamagnetic suppression of component magnetic reconnection at the magnetopause. *Journal of Geophysical Research*, *108*(A5), 1218. https://doi.org/10.1029/2002JA009726

Torbert, R. B., Burch, J. L., Argall, M. R., Alm, L., Farrugia, C. J., Forbes, T. G., et al. (2017). Structure and dissipation characteristics of an electron diffusion region observed by MMS during a rapid, normal-incidence magnetopause crossing. *Journal of Geophysical Research: Space Physics*, *122*, 11,901–11,916. https://doi.org/10.1002/2017JA024579

Torbert, R. B., Burch, J. L., Giles, B. L., Gershman, D., Pollock, C. J., Dorelli, J., et al. (2016). Estimates of terms in Ohm's law during an encounter with an electron diffusion region. *Geophysical Research Letters*, *43*, 5918–5925. https://doi.org/10.1002/2016GL069553

Torbert, R. B., Burch, J. L., Phan, T. D., Hesse, M., Argall, M. R., Shuster, J., et al. (2018). Electron-scale dynamics of the diffusion region during symmetric magnetic reconnection in space. *Science*, *362*, 1391–1395. https://doi.org/10.1126/science.aat2998

Wang, S., Chen, L.-J., Bessho, N., Hesse, M., Yoo, J., Yamada, M., et al. (2018). Energy conversion and partition in the asymmetric reconnection diffusion region. *Journal of Geophysical Research: Space Physics*, *123*, 8185–8205. https://doi.org/10.1029/2018JA025519

Wang, S., Chen, L.-J., Bessho, N., Kistler, L. M., Shuster, J. R., & Guo, R. (2016). Electron heating in the exhaust of magnetic reconnection with negligible guide field. *Journal of Geophysical Research: Space Physics*, *121*, 2104–2130. https://doi.org/10.1002/2015JA021892

Webster, J. M., Burch, J. L., Reiff, P. H., Daou, A. G., Genestreti, K. J., Graham, D. B., et al. (2018). Magnetospheric multiscale dayside reconnection electron diffusion region events. *Journal of Geophysical Research: Space Physics*, *123*, 4858–4878. https://doi.org/10.1029/2018JA025245

Wilder, F. D., Ergun, R. E., Burch, J. L., Ahmadi, N., Eriksson, S., Phan, T. D., et al. (2018). The role of the parallel electric field in electron-scale dissipation at reconnecting currents in the magnetosheath. *Journal of Geophysical Research: Space Physics*, *123*, 6533–6547. https://doi.org/10.1029/2018JA025529

Wilder, F. D., Ergun, R. E., Eriksson, S., Phan, T. D., Burch, J.-L., Ahmadi, N., et al. (2017). Multipoint measurements of the electron jet of symmetric magnetic reconnection with a moderate guide field. *Physical Review Letters*, *118*, 265101. https://doi.org/10.1103/PhysRevLett.118.265101

Yoon, P. H., & Lui, A. T. Y. (2005). A class of exact two-dimensional kinetic current sheet equilibria. *Journal on Geophysics Research: Space Physics*, *110*, A01202. https://doi.org/10.1029/2003JA010308

Yordanova, E., Vörös, Z., Varsani, A., Graham, C., Norgren, Y. V., Khotyaintsev, A., et al. (2016). Electron scale structures and magnetic reconnection signatures in the turbulent magnetosheath. *Geophysics Research Letters*, *43*, 5969–5978. https://doi.org/10.1002/2016GL069191